Journal of Crystal Growth 401 (2014) 418–422

Contents lists available at ScienceDirect

Journal of Crystal Growth

journal homepage: www.elsevier.com/locate/jcrysgro

The subgrain structure in turbine blade roots of CMSX-4 superalloy

Włodzimierz Bogdanowicz [a], Robert Albrecht [a,*], Jan Sieniawski [b], Krzysztof Kubiak [b]

[a] Institute of Material Science, University of Silesia, Bankowa 12, 40-007 Katowice, Poland
[b] Department of Material Science, Rzeszów University of Technology, W. Pola 2, 35-959 Rzeszów, Poland

ARTICLE INFO

Available online 7 December 2013

Keywords:
A1. X-ray topography
B1. Superalloys
B3. Turbine blades

ABSTRACT

As-cast single-crystal turbine blade roots made of CMSX-4 were investigated. The Laue method, X-ray diffraction topography, novel X-ray diffractometer provided by EFG company and scanning electron microscopy were applied to study the subgrain structure. It was found that low angle boundaries of macro scale length were present in the roots of the blades. Additionally, linear distributions of angles describing inclination of $[001]_{\gamma'}$ direction to the main blade axis and rotation of this direction were defined across the low angle boundaries by EFG diffractometer. With the use of this diffractometer, the lattice parameter linear distributions across the low angle boundaries were also defined. The dendrites arrangement were determined by scanning electron microscopy (SEM) macro images. The mechanism of the formation of subgrain boundaries and characteristics of the orientation interactions between dendrites inside subgrains were proposed.

1. Introduction

Single-crystal nickel-base superalloys are widely used as material for turbine blades in advanced aircraft engines and stationary gas turbines [1]. As these elements are critical for flight safety, much attention should be given for preventing casting defects. However, dendritic structure, complex shape and chemical composition of turbine blades tend to create many growth defects. Therefore, investigation of the real structure of the turbine blades is fundamental in the prevention of damage during service. In industrial directional solidification of single crystalline blades, the formation of macro scale defects such as freckles or random grains, are well known and could be limited by appropriate solidification parameters [2–5]. Despite this, formation of macro scale subgrains is possible during solidification and after further processing [6].

Single crystal superalloys are not strictly single crystal. In fact, they are a set of dendrites solidified in the same crystal orientation. Additionally, each dendrite generally consists of two phases: γ and γ′, where γ′ in the form of cubic crystals located mostly in the dendritic cores and fills about 70% (vol) of the alloy. However, at macro scale this material exhibits the features characteristic to the single crystal [6]. Because of the complex character of macro and micro subgrain structures in single crystal superalloys, their precise characterization is still not sufficient. Single crystal turbine blades are produced by directional solidification investment casting with heat transfer along *Z* axis of the blade (Fig. 1a). Crystallization of single crystal is achieved through the spiral selector, which allows one grain to survive, and enter the root section of the blade, then to airfoil. The widening of the crystallization front at the transition to root generates many solidification defects [7,8]. These defects are then inherited by the airfoil, the most loaded part of the blade. Therefore, the complex analysis of the root section is very important. Particularly important are crystal misorientation defects as they possess high influence on creep strength during service.

The focus of this study was the macro scale characterization of subgrain structure of as-cast single crystal turbine blades roots, made of CMSX-4 superalloy, with precise investigation of crystal misorientation parameters. Although, recently many research were conducted to characterize misorientation defects by SEM Electron Backscattered Diffraction (EBSD) technique [9,10] none of them define precise misorientation (minutes of arc) parameters.

2. Experimental

For the investigation, twelve single crystal blades were solidified using an ALD industrial furnace at the Research and Development Laboratory for Aerospace Materials of the Rzeszów University of Technology, Poland. Certificated industrial nickel based superalloy CMSX-4 was used in the experiment. The nominal chemical composition in wt% was as follows: 5.6 Al, 1.0 Ti, 6.5 Ta, 6.5 Cr, 0.6 Mo, 6.0 W, 9.0 Co, 3.0 Re, 0.1 Hf, less 0.002 C, Ni bal. The dominant phase in CMSX-4 superalloy was γ′ [11]. The blades, shape of which present in Fig. 1a, were solidified directionally by the vertical Bridgeman technique at the withdrawal rate of 3 mm/min and thermal gradient about 15 K/mm.

* Corresponding author at: Institute of Materials Science, University of Silesia, ul. Pułku Piechoty 1A, 41-500 Chorzów, Poland. Tel.: +48 32 349 75 36.
E-mail addresses: wlodzimierz.bogdanowicz@us.edu.pl (W. Bogdanowicz), ralbrecht@us.edu.pl (R. Albrecht), jansien@prz.edu.pl (J. Sieniawski), krkub@prz.edu.pl (K. Kubiak).

0022-0248/$ - see front matter © 2013 Elsevier B.V. All rights reserved.
http://dx.doi.org/10.1016/j.jcrysgro.2013.11.092

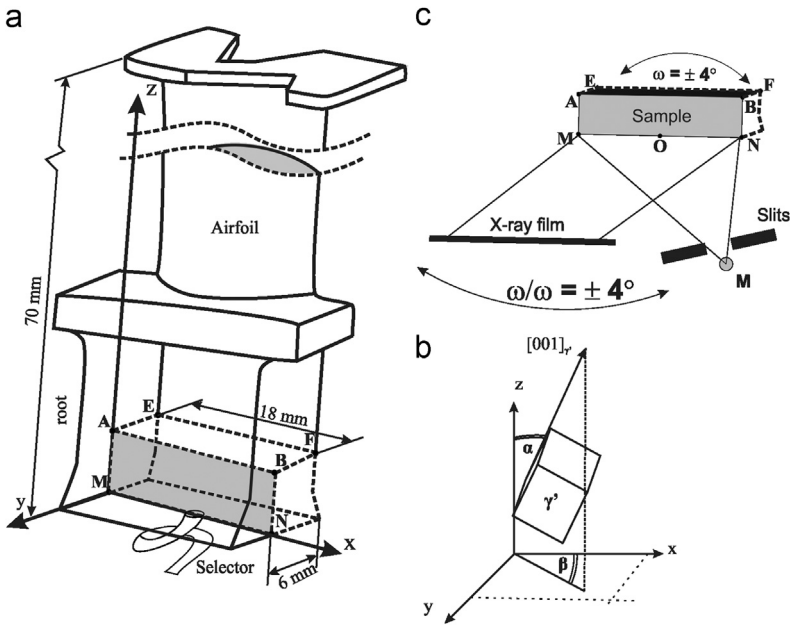

Fig. 1. Scheme of the samples location (a), method of determining misorientation angles α, β (b) and scheme of obtaining X-ray topograms (c). ABNM—sample surface for investigation (gray); O—the axis of oscillation film and sample; M—X-ray microfocus source.

The samples with surface parallel to the *ZX* plane (Fig. 1a, surface ABNM at connection of selector with root) were prepared from each root of the blades. The set of X-ray methods consisted of X-ray diffraction topography, Laue diffraction and X-ray diffraction mapping [6] were used.

X-ray diffraction mapping of all samples was conducted on novel diffractometer apparatus provided by EFG company (Berlin, Germany). With the use of 1 mm spot size incident beam in the diffractometer, the obtained diffractions were compared to stored data and, on this basis, angle α (determining inclination of $[001]_{\gamma'}$ direction to the *Z* axis, Fig. 1b) and β (rotation of $[001]_{\gamma'}$ direction about *Z* axis), and lattice parameter a_0 of γ′ from each point were calculated, creating maps of distribution. From the maps of α and β components and the lattice parameter, their linear distributions (α(x), β(x), a_0(x)) across the subgrain boundary were determined. The dendritic arrangements were visualized for each sample by JEOL JMS 6480 scanning electron microscope (SEM) via stitching 20 images to macro image of surfaces ABMN (Fig. 1a). Additionally, all samples were oriented by the Laue method and then the X-ray reflective topograms were obtained from the same surfaces. By the Laue method it was stated that the [001]γ′ direction was circa parallel to the *Z* blade axis.

The X-ray topography system was equipped with new micro-focus Cu source (Panalytical) and an Aulytner camera [12]. The X-ray reflective topography were used with divergent beam (Fig. 1c) and with coupled sample/film oscillation [12]. Topograms were recorded on X-ray film with the usage of 220 $Cu_{K\alpha}$ reflection of phase γ′.

3. Results

Fig. 2 shows the dendritic structure at macro scale of the sample obtained by the BSE technique on SEM. Due to the difference in phase composition between the dendritic and inter-denritic region, the BSE technique allows to observe the arrangement of dendrite arms on the sample surface without etching. The same surface was examined via X-ray topography (Fig. 3). From SEM macro images of the whole surface (Fig. 2), it was determined that on the output of selector, secondary dendrite arms (SDA) spread about horizontal (almost parallel to *x* axis) and became the base for tertiary dendrite trunks (TDT). The SEM macro image presented on Fig. 1 can be divided into three areas: SA (selector area), A (left dendrite trunk) and B (right dendrite trunk). In A and B areas close to the bottom edge MN of the sample the long secondary dendrite arms (SDA) going through whole areas are visible, while in SA area this type of dendrite arms is not present. From this image, the inclinations to the *Z* axis of primary dendrite trunks of region SA and tertiary from regions A and B were determined. In regions A and SA dendrites were inclined at 3 degrees (δ_A, δ_{SA}). In the B region, dendrite trunks were inclined at 2,2 degrees (δ_B). At the bottom of the sample (below lines RF and MN of A and B regions), where the crystallization continues with the participation of secondary dendrite arms (SDA), dendrites (Fig. 1, filled thick arrows), the growth of which was cut (probably by neighbors), can be seen. Additionally, the highest density of dendrites can be found in subarea D of B area.

Fig. 3 presents the X-ray reflection topogram obtained from the surface which dendritic structure is presented in Fig. 2. It is clearly visible that the contrast bands are distorted in comparison to straight lines of dendrite cores observed in Fig. 2. The topogram can be divided into three main areas: I, II, and III. Area I on the topogram contains four subgrains marked as J^1, J^2, J^3, and J^4. Area II is the subgrain with the misorientation described by shifts Δz relative to the area III—which is the subgrain III (Fig. 3). The shifts Δz are the same for each dendrites within subgrain II. The D subarea on topogram indicates the place of high density of small dendrite arms showed on Fig. 2. The C area indicates the part of subgrain II with some misorientation in relation to all dendrites from subgrain II (C is shifted from C′). Additionally, area I on topogram could be divided into 4 subareas marked as J^1, J^2, J^3, and J^4, which can be considered as additional subgrains.

Fig. 4 presents linear distributions of angles α and β and the lattice parameter a_0 of the γ′ phase across the low angle boundary (along the segment m_1m_2 parallel to the *x* axis). It was found that α changed about 0.4 degrees and β change about 4 degrees between subgrains II and III (Fig. 4a and b). Linear distributions of the lattice parameter (Fig. 4c) reveal its small reduction at low angle boundaries

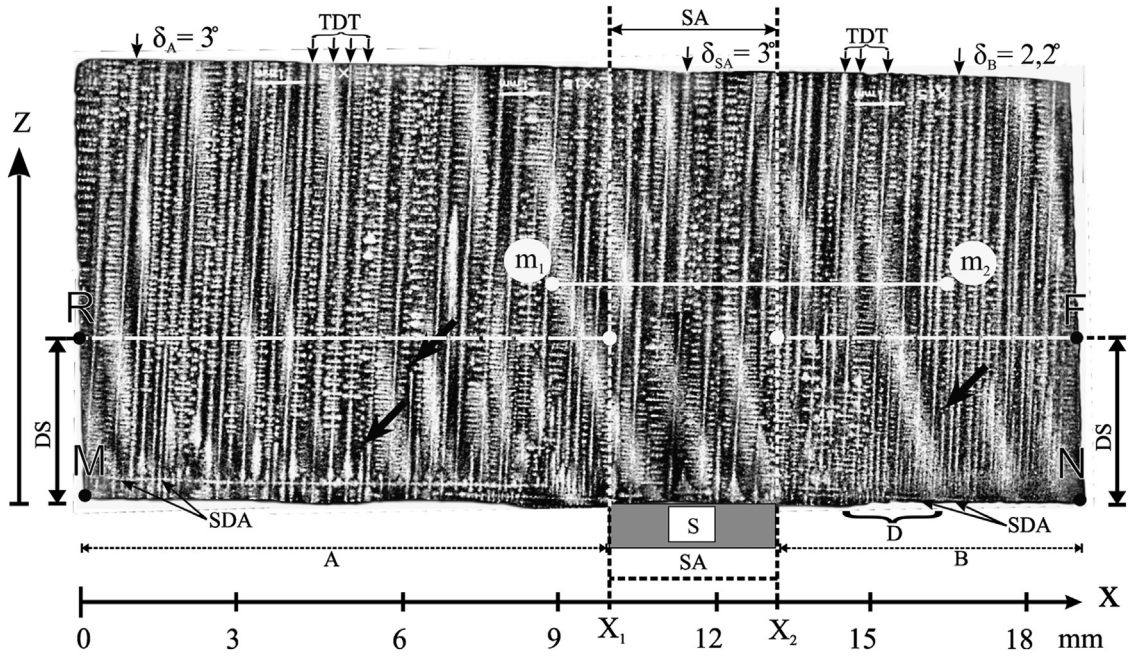

Fig. 2. Typical SEM image of dendrite structure visualized on the sample surface. BSE technique. S—selector, SA—selector area of root. A, B—areas of growth from secondary dendrite arms. DS (distortion area)—area of competitive dendrite growth. *Z*—main blade axis (solidification direction). SDA—secondary dendrite arms, TDT—tertiary dendrite trunks.

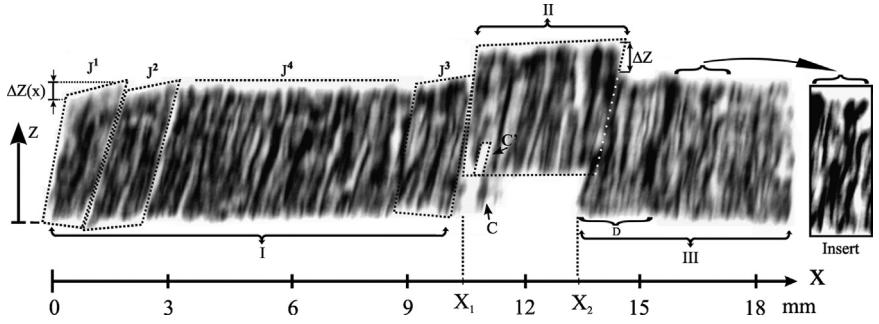

Fig. 3. Typical X-ray topogram of ABNM sample surface. $Cu_{K\alpha}$ 220 γ′ reflection.

between J^3 and subgrain II, as well as between subgrains II and III (arrows with on Fig. 4c).

4. Discussion

From macro scale SEM images it is shown that within DS area of A and B areas (Fig. 2) the growth of some dendrites could be cut. It is probably caused by fast growth of secondary dendrite arms of neighbor dendrites.

This can prove that competitive growth of dendrites is possible in the turbine blade root (Fig. 2, DS area). Moreover, the spread of secondary dendrite arms (SDA, Fig. 2) when crystallization reached the wider region of the mold (transition from selector S to root part of MN wide, Fig. 2) can initiate a change of growth direction of tertiary dendrite arms (TDT, Fig. 2) and, thus, formation of macro low angle boundaries. Examination of the occurrence of low angle boundaries by SEM investigation is very difficult (the subgrain boundaries are not visible on Fig. 2). As a result, in order to achieve proper analysis of the subgrain structure, the X-ray topography or linear distributions of angle α and β should be applied. The ref. [13] provides information that only primary dendrite arms possess fine oriented structure and secondary dendrite arms are highly misoriented as well as possessing many micro subgrains. Location on the *x*-axis of subgrain II boundaries (X_1;X_2) on the topogram is correlated with boundaries of SA area, on which long secondary dendrite arms are not present. However, long SDA is present in the A and B areas (Fig. 2). On the topogram (Fig. 3) areas I and III, which correspond to the macro SEM (Fig. 2) A and B areas, are shifted in respect to area II. This indicates that these areas are misoriented in respect to SA area–area where dendrites growth are continued directly from selector. On the other hand, in A and B areas tertiary dendrite arms grown from secondary dendrite arms (SDA, Fig. 2). It could be stated that with resolution of used topography equipment, single contrast band (Fig. 3, Inset) on topogram are the reflection from individual dendrite where the most volume of γ′ (which reflection creates topogram) is located at as-cast state. From this follows we suggest that the occurrence of misorientation inherited from growth of secondary dendrite arms is highly possible. Moreover, contrast bands from dendrite cores on the topogram are bent in *Z* axis (Fig. 3, Inset) which proves that fluctuations of orientation in these dendrite arms occurred during solidification. The inner structure of macro scale subgrains (J^1, J^2, J^3, J^4, II and III) in single crystal

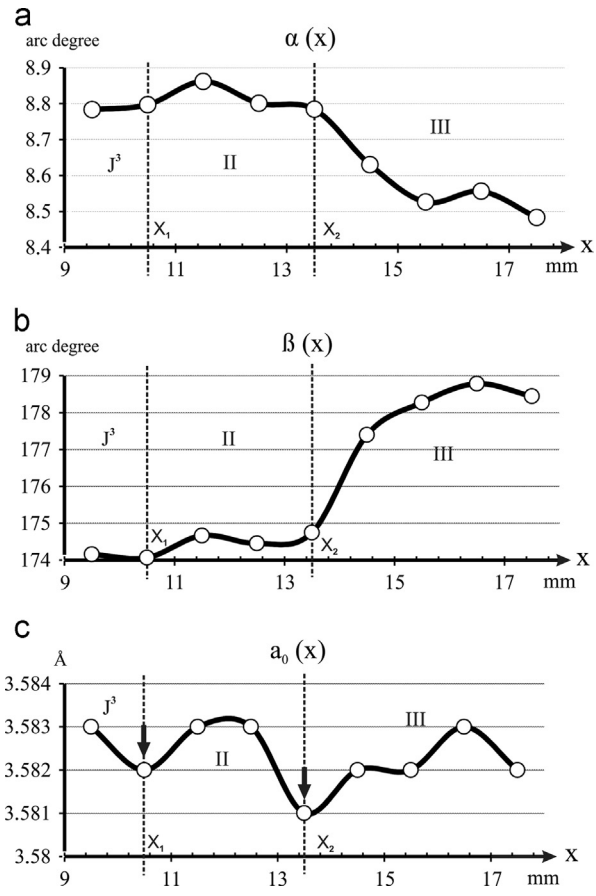

Fig.4. Distribution of α (a) and β (b) angles and lattice parameter a_0 (c) along *x*-axis.

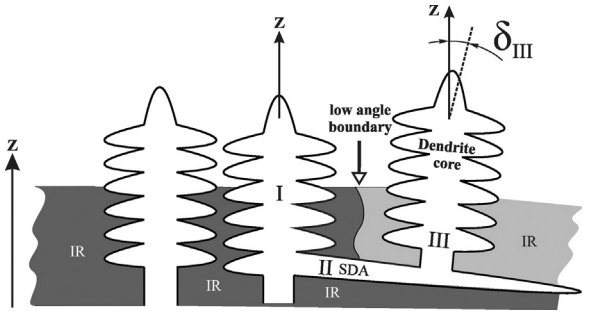

Fig. 5. Scheme of location and formation of low angle boundary. IR—interdendritic region. I, II, and III dendrite arms rank. δ_{III}–angles between dendrite and *Z* axis.

dendritic superalloys is more complex in comparison with strict single crystals. This forces a need to implement new terms and new classifications for its description. Therefore, it seems reasonable to use the term "orientation structure" of single crystal dendritic superalloys. This structure can be visualized by X-ray diffraction topography.

From the topogram (Fig. 3) it is concluded that the subgrains of the macro scale dimension could be divided in two types. The first is that inside which misorientation between neighbor dendrites is generally not observed (subgrain II and III). In this case, shift of the whole subgrain image is observed on the topogram (Fig. 3, ΔZ shift between subgrains II and III). In such type of subgrains, orienting interaction between primary dendrite trunks, which keep the whole subgrain orientation uniform, are strong. The second type is one in which the continuous change of shift of each neighbor dendrite image within subgrain occurred (Fig. 3, J^1, J^2, J^3 – $\Delta z(x)$ is a monotonic function of x). In this case, it could be indicate that the orienting interactions between dendrites are weak.

The analysis of the graphs presented on Fig. 4 shows that relation α(x), β(x) and a_0 revels noticeable changes in points X_1 and X_2. The values of X_1 and X_2 correspond with the position of the subgrain boundaries J^3-II and II-III from Fig. 3. α(x), β(x) changes in X_1 and X_2 prove the existence of subgrain boundaries. The boundary between II and III subgrain have higher misorientation values (higher α and β changes) then boundary between J^3 and II. The lower values of J^3-II boundary misorientation can be caused by gradually misorientation changes within J^3. For $a_0(x)$ relation we can observe decrease in lattice parameter at X_1 and X_2 points, which probably is the result of chemical composition changes at low angle boundaries location.

The newest research [14] provides the conclusion of inherited orientation from primary dendrite arms by the interdendritic (IR) region. Additionally, the IR region accumulates many growth defects during crystallization [15]. We propose to extend the scheme with the possibility to create the low angle boundary in case of dendrite cores misorientation occurs.

Fig. 5 shows the scheme of formation of macro scale low angle boundaries during crystallization of 3rd-rank dendrite arms. During crystallization at the wider part of the mold, secondary dendrite arms (Fig. 2, SDA) give the base for further growth in the areas A and B (Fig. 2). However, because of the inner mosaic structure (micro subgrain inside each SDA [6]) they tend not to grow perpendicularly to the primary dendrites. Dendrite cores growing from this inclined secondary arms change their grow directions ($\delta_{III} \neq 0$). This direction change is then imposed to the interdendritic region, in which the low angle boundary of macro scale is formed. The boundary is located in the IR region between I and III misorientated dendrite cores (Fig. 5) and could grow through the entire cast. Decrease in withdrawal rates during solidification front passing through selector–root sections could prevent such defects.

5. Conclusions

Methodology

1. The X-ray topography and diffraction mapping obtained on EFG diffractometer prove to be sufficient methods, which when used together, significantly improve precise macro scale misorientation investigation in dendritic single crystal superalloys.
2. Due to the complex structure of misorientation within and between single dendrites, we suggest to use the term "orientation structure" for describing details of misorientation in dendritic single crystal superalloys.

Materials

3. The competitive growth of primary dendrite arms is possible in root at some distance after crystallization pass through selector.
4. Macro scale low angle boundaries formation could be initiated in the areas of crystallization front extension (selector–root part passage). This could be caused by inclined growth of secondary dendrite arms resulting in misoriented growth of further tertiary dendrite arms.
5. Formation of macro scale low angle boundaries disturb lattice parameters probably due to element segregation around boundaries.
6. There are two types of orienting interactions between neighbor dendrites inside the subgrain:
   – Strong, when the crystal orientation of each dendrite within subgrain are the same.

– Weak, when misorientation monotonically changes for each subsequent neighboring dendrite within subgrain.

Acknowledgment

The research was financed by the Polish National Centre for Research and Development (NCBiR) under Grant no. INNOTECH-K2/IN2/57/182858/NCBR/13.

References

[1] R.C. Reed, The Superalloys:Fundamentals and Applications, Cambridge University Press, 2006.
[2] S. Tin, T.M. Pollock, Predicting freckle formation in single crystal Ni-base superalloys, J. Mater. Sci. 11 (2004) 7199–7205.
[3] D. Ma, J. Ziehm, W. Wang, A. Bührig-Polaczek, Freckle formation in directionally solidified superalloy components with expanding cross-section, Mater. Sci. Eng 27 (2011).
[4] Y. Amouyal, D.N. Seidman, The role of hafnium in the formation of misoriented defects in Ni-based superalloys: an atom-probe tomographic study, Acta Mater. 59 (2011) 3321–3333.
[5] L. Yang, P.D. Lee, A new mechanism for freckle initiation based on microstructural level simulation, Acta Mater. 60 (2012) 4917–4926.
[6] W. Bogdanowicz, R. Albrecht, A. Onyszko, J. Sieniawski, Characterization of single-crystal turbine blades by X-ray diffraction methods, Solid State Phenom. 203–204 (2013) 63–66.
[7] X. Zhang, Y. Zhou, Y. Han, T. Jin, X. Sun, Dendritic growth pattern and dendritic network distortion in the platform of a Ni-based superalloy, J. Mater. Sci. Technol. http://dx.doi.org/10.1016/j.jmst.2013.09.013, in press.
[8] X.B. Meng, J.G. Li, Z.Q. Chen, Y.H. Wang, S.Z. Zhu, X.F. Bai, F. Wang, J. Zhang, T. Jin, X.F. Sun, Z.Q. Hu, Effect of platform dimension on the dendrite growth and stray grain formation in a ni-base single-crystal superalloy, Metal. Mater. Trans. A 44A (2012) 1955–1965.
[9] H. Hao, W. Jiang, G. Xie, G. Zhang, Y. Lu, J. Zhang, L. Lou, Microstructure and grain orientation evolution of a specially shaped shroud during directional solidification process, Prog. Nat. Sci. 23 (2013) 211–215.
[10] J.W. Aveson, P.A. Tennant, B.J. Foss, B.A. Shollock, H.J. Stone, N. D'Souza, On the origin of sliver defects in single crystal investment castings, Acta Mater. 61 (2013) 5162–5171.
[11] J.R. Davis, Heat Resistant Materials, Materials Park: ASM International, USA, 1997.
[12] W. Bogdanowicz, Martensitic transformations in β1-CuZnAl single crystals studied by X-ray topography method, Scripta Mater 37 (1997) 829–835.
[13] U. Bruckner, A. Epishin, T. Link, Local X-ray diffraction analysis of the structure of dendrites in single-crystal nickel-base superalloys, Acta Mater. 45 (1997) 5223–5231.
[14] J.W. Aveson, G. Reinhart, H. Nguyen-Thi, N. Mangelinck-Noël, A. Tandjaoui, B. Billia, K. Goodwin, T.A. Lafford, J. Baruchel, H.J. Stone, D'Souza, Dendrite bending during directional solidification, Superalloys (2012) 4715–4723.
[15] N.S. Husseini, D.P. Kumah, J.Z. Yi, C.J. Torbet, D.A. Arms, E.M. Dufresne, T.M. Pollock, J.W. Jones, R. Clarke, Mapping single-crystal dendritic microstructure and defects in nickel-base superalloys with synchrotron radiation, Acta Mater. 56 (2008) 4715–4723.